Journal of Colloid and Interface Science 638 (2023) 640–649

Contents lists available at ScienceDirect

Journal of Colloid and Interface Science

journal homepage: www.elsevier.com/locate/jcis

Dual functionality luminescence thermometry with $Gd_2O_2S:Eu^{3+},Nd^{3+}$ and its multiple applications in biosensing and in situ temperature measurements

Yixuan Ma [a], Abida Aierken [b], Yuhua Wang [a,*], Andries Meijerink [a,c,*]

[a] National and Local Joint Engineering Laboratory for Optical Conversion Materials and Technology of National Development and Reform Commission, Lanzhou University, Lanzhou, 730000, China
[b] School of Stomatology, Lanzhou University, Lanzhou 730000, China
[c] Condensed Matter and Interfaces, Debye Institute for Nanomaterials Science, Utrecht University, Princetonplein 1, 3584CC Utrecht, the Netherlands

GRAPHICAL ABSTRACT

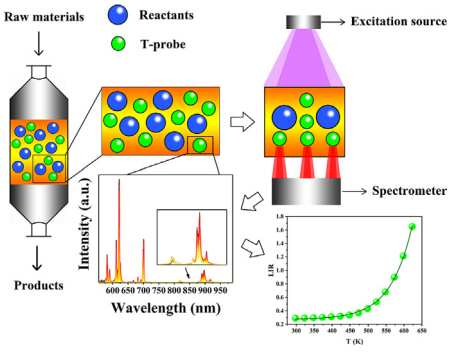

ARTICLE INFO

Article history:
Received 16 December 2022
Revised 25 January 2023
Accepted 4 February 2023
Available online 8 February 2023

Keywords:
Luminescence thermometer
Sensitizer
Near-infrared thermography
Temperature-dependent spectroscopy
Physiological sensing
In situ temperature measurements
Sensors

ABSTRACT

Luminescence thermometry using sharp line emission of lanthanide ions has become an active area of research as it offers the advantages of remote temperature sensing with high sensitivity and superior spatial resolution. The most widely applied method relies on the temperature dependence of the luminescence intensity ratio of emission lines from two thermally coupled levels. However, the usable temperature range for this type of Boltzmann thermometer is limited. In addition, the weak and narrow line absorption of the parity forbidden 4f-4f transitions of lanthanides forms a serious drawback. To solve both problems, we here report a new dual functionality luminescence thermometer: Gd_2O_2S co-doped with Eu^{3+} and Nd^{3+}. This material combines Boltzmann and energy transfer thermometry to extend the temperature range and uses the strong and broad charge transfer absorption band of Eu^{3+} for sensitization. In the *T*-range of 300–500 K efficient energy transfer from Eu^{3+} to Nd^{3+} allows for charge transfer-sensitized luminescence thermometry using near infrared emission from the thermally coupled $^4F_{3/2}$ and $^4F_{5/2}$ levels of Nd^{3+}. Above 500 K a high temperature sensitivity is obtained using the strong temperature dependence of the luminescence intensity ratio of red Eu^{3+} to near infrared Nd^{3+} emission. The dual-functionality provides a single thermometer combining strong absorption and high relative sensitivity (0.6 – 1.4%) over a wide temperature range (300 to 650 K). Finally, it is proposed that this dual-function luminescent thermometer has promising potential for multifunctional applications in biosensors and in situ temperature measurements of chemical reaction process.

* Corresponding authors.
E-mail addresses: wyh@lzu.edu.cn (Y. Wang), a.meijerink@uu.nl (A. Meijerink).

https://doi.org/10.1016/j.jcis.2023.02.022
0021-9797/

1. Introduction

Temperature is the most frequently measured physical parameter and is of wide interest both in scientific research and in the world around us. The importance of temperature and its accurate measurement is crucial in many fields, such as aerospace and defense, bio-medicine, microfluidics, electronic devices and temperature variations in chemical reactors [1–8]. In line with the vital role of temperature, new methods and new types of temperature sensors are continuously developed to improve ease of use, reliability, accuracy and spatial resolution. Traditionally, contact temperature probes were used that are based on the thermal expansion of liquids, temperature variation of the resistance of metals or the thermoelectric effect in thermocouples [2,9]. However, when the spatial resolution of the system to be measured reaches the micron or even nanometer level, the application of conventional contact temperature probes is greatly limited [7,10–17].

An alternative approach is a non-invasive technique by remotely monitoring the temperature-dependent emission spectrum of a luminescent probe. A variety of temperature dependent luminescence properties can be used, including spectral shift, luminescence lifetime, bandwidth, polarization, intensity, and luminescence intensity ratio (LIR) [18]. Among all methods, especially the LIR measurement is a very robust and reliable method due to its independence from changes in experimental conditions such as sample alignment and intensity variations due to changes in e.g. absorption or light scattering [19,20]. Specifically, lanthanide ion-doped luminescence thermometry based on the emission from two thermally coupled energy levels has been widely explored for accurate temperature-sensing [21,22]. The sharp emission lines of the $4f^n \rightarrow 4f^n$ (f-f) intra-configurational transitions of lanthanide ions allow for precise determination of the emission intensity from the two levels. Accuracies down to 0.1 K can be achieved. As a result lanthanide ion luminescence thermometry is rapidly developing with the advantages of non-invasiveness, high sensitivity, accuracy and reproducibility and superior temporal and spatial resolution.

Emission from lanthanide ions is characterized by high quantum yields but the parity forbidden f-f transitions have low absorption strengths which often necessitates the use high excitation power, causing undesired (laser) heating [23,24]. In addition, Boltzmann thermometry relying on the variation of emission intensity from two thermally coupled levels works well, but only in a limited temperature range [25]. In this paper we address both problems: lanthanide emission is sensitized by the introduction of a sensitizer ion to greatly increase the brightness while the temperature range is extended by exploring dual functionality using the LIR from thermally coupled levels at low temperatures and the LIR from sensitizer/activator emission in the high temperature regime. Note that it is not easy to find a good sensitizer in luminescence (nano)thermometry. A good sensitizer ion shows strong absorption resulting from a parity allowed transition, followed by efficient energy transfer to the activator. Typical sensitizers are Ce^{3+} and Eu^{2+} with parity allowed $4f^n$–$4f^{n-1}5d$ transitions. However, for both ions often the energy transfer efficiency to parity forbidden f-f transitions is low. For Eu^{2+}, in addition there is an experimental incompatibility with nanocrystals. Reducing synthesis conditions are required and this limits ability to incorporate Eu^{2+} in nanocrystals. Previous reports on Eu^{2+} in nanocrystals indicate that besides Eu^{2+} there is always Eu^{3+} present [26].

Here we use the well-known Gd_2O_2S matrix as host. Oxysulfides are widely used in phosphors, X-ray imaging systems and up-conversion luminescence [27,28] because of their high luminescence efficiency, high chemical stability and low phonon energy. The bright emission for Eu^{3+} in the gadolinium oxysulfide lattice originates from the strong UV charge-transfer (CT) absorption extending to the edge of the visible region around 400 nm. Note that cheap and powerful near-UV diodes and diode-lasers in this wavelength range are readily available. We here use the strong broad band CT absorption to sensitize the emission of Nd^{3+}. The LIR of the $^4F_{3/2}$-$^4F_{5/2}$ emission from Nd^{3+} is well-known for luminescence thermometry. The energy difference ΔE for these two energy levels is around 1000 cm^{-1}. They are thermally-coupled (in Boltzmann equilibrium) starting at temperatures around/just above room temperature [29]. By co-doping with Eu^{3+} we aim to utilize the strong CT absorption of Eu^{3+} in the near-UV to enhance brightness and to use the LIR of Eu^{3+} to Nd^{3+} emission in the high temperature range where the change in LIR of the $^4F_{3/2}$-$^4F_{5/2}$ becomes small.

To explore the feasibility of this dual-functionality LIR thermometer, the luminescence properties of Gd_2O_2S:Nd^{3+} as well as Gd_2O_2S:Eu^{3+},Nd^{3+} were studied for different doping concentrations to validate and optimize the effectiveness of energy transfer from Eu^{3+} to Nd^{3+}. Next, the temperature dependence of the $^4F_{3/2}$-$^4F_{5/2}$ emission LIR in Gd_2O_2S:Nd^{3+} and the Eu^{3+}/Nd^{3+} emission LIR in Gd_2O_2S:Eu^{3+},Nd^{3+} were studied. For Gd_2O_2S:Nd^{3+} the temperature-dependent LIR based on Boltzmann equilibrium results in accurate temperature sensing capabilities up to $\sim$ 500 K. In the co-doped Gd_2O_2S:Eu^{3+},Nd^{3+} system effective sensitization of Nd^{3+} emission by Eu^{3+} is realized upon Eu^{3+} CT excitation. The co-doped sample shows greatly improved sensitivity and expands the temperature range beyond 650 K by combining Boltzmann thermometry with the temperature dependent Eu^{3+} to Nd^{3+} luminescence intensity ratio. Based on the excellent temperature sensing properties of the proposed material, we present the possibility of multifunctional applications of one material in different fields. The results show that our new dual-functionality luminescence thermometer has promising applications in biological thermometry applications as well as in situ temperature monitoring of chemical reaction processes.

2. Results and discussion

Structure and morphology. The oxysulfides were prepared using standard solid state synthesis techniques [30,31]. The XRD patterns of all prepared materials Gd_2O_2S: xNd^{3+} (x = 0.002, 0.005, 0.008, 0.010, 0.015) with different doping concentrations of Nd^{3+} and Gd_2O_2S:yEu^{3+}, 0.008Nd^{3+} (y = 0.005, 0.008, 0.010, 0.015, 0.020) with different concentrations of Eu^{3+}, refinement results of matrix and the morphological analysis are detailed in the Supporting Information section. High quality single phase microcrystalline material was obtained.

Luminescence Properties and Energy Transfer. To investigate the luminescence properties, photoluminescence excitation (PLE) and emission spectra (PL) were recorded at room temperature, first for the singly Nd-doped material. As an example Fig. 1**(a)** shows the normalized excitation and emission spectra of the Gd_2O_2S:0.008Nd^{3+}. The excitation spectrum (blue line) is monitored for the dominant Nd^{3+} emission at 900 nm. Narrow excitation lines are observed characteristic of Nd^{3+} and consistent with the well-known energy level diagram of Nd^{3+}. The strongest excitation lines around 600 nm originate from transitions to the $^2H_{11/2}$ and $^2G_{5/2}$, $^4G_{7/2}$ excited states. The emission spectrum (red line) for excitation at 601 nm shows the characteristic NIR emission from Nd^{3+} with two distinct peaks centered around 823 nm and 900 nm. These peaks correspond to the $^4F_{5/2}\rightarrow{}^4I_{9/2}$ and $^4F_{3/2}\rightarrow{}^4I_{9/2}$ transitions of Nd^{3+}, respectively, as shown in Fig. 1**(a)**. The intensity of the $^4F_{5/2}\rightarrow{}^4I_{9/2}$ emission is low at room temperature since thermal

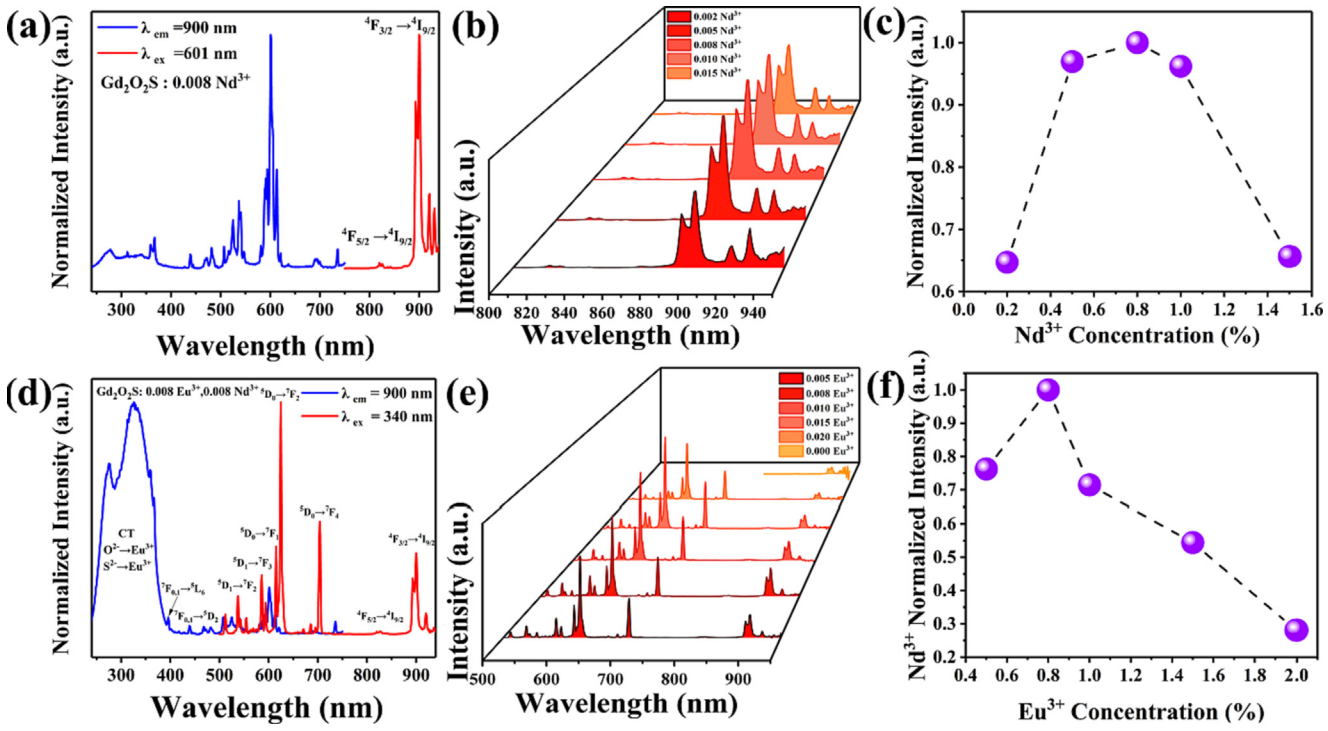

Fig. 1. (a) Photoluminescence excitation (PLE) and emission (PL) spectra of Gd_2O_2S:0.008Nd^{3+}. (b) Emission spectra of Gd_2O_2S: xNd^{3+} (x = 0.002, 0.005, 0.008, 0.010, 0.015) samples doped with various Nd^{3+} concentrations. (c) Changing trend of peak emission intensity with different Nd^{3+} doping concentrations. (d) PLE and PL spectra of Gd_2O_2S: 0.008Eu^{3+}, 0.008Nd^{3+}. (e) Emission spectra of co-doped Gd_2O_2S: yEu^{3+}, 0.008Nd^{3+} (y = 0.000, 0.005, 0.008, 0.010, 0.015, 0.020). (f) Concentration dependence of the Nd^{3+} emission intensity of co-doped samples Gd_2O_2S:yEu^{3+}, 0.008Nd^{3+} (y = 0.005, 0.008, 0.010, 0.015, 0.020)).

population of the $^4F_{5/2}$ level at 300 K is small given the size of the $^4F_{5/2}$ - $^4F_{3/2}$ energy gap of ~ 1000 cm^{-1}.To optimize the Nd^{3+} concentration emission spectra of Gd_2O_2S: xNd^{3+} (x = 0.002, 0.005, 0.008, 0.010, 0.015) samples were recorded as shown in Fig. 1**(b)**. The integrated emission intensity is plotted as function of x in Fig. 1**(c)**. The highest emission intensity is measured a Nd-doping concentration of 0.008. At higher doping concentrations the probability for cross-relaxation quenching of the $^4F_{3/2}$ emission increases, causing a drop in intensity [32].

In order to solve the problem of the weak absorption strength of the parity forbidden Nd^{3+} $4f^n \rightarrow 4f^n$ transitions, Eu^{3+} was introduced as a sensitizer ion with a strong absorption. Note that Eu^{3+} is not often used as a sensitizer because typically it also has weak narrow absorption lines in the visible and near-UV spectral region. However, in the Gd_2O_2S matrix lattice Eu^{3+} shows very strong charge transfer absorption in the near-UV which can be easily excited using cheap near-UV diode excitation sources. If, following CT absorption and relaxation to the $^5D_0$ level, efficient energy transfer can occur from Eu^{3+} to nearby Nd^{3+} ions, sensitization of Nd^{3+} emission is realized.

To investigate the sensitization scheme outlined above, Gd_2O_2S co-doped with Eu^{3+} and Nd^{3+} was investigated. Fig. 1**(d)** shows the excitation and emission spectra of Gd_2O_2S:0.008Eu^{3+}, 0.008Nd^{3+}. The excitation spectrum (blue line) was recorded again monitoring the dominant Nd^{3+} $^4F_{3/2}\rightarrow{}^4I_{9/2}$ transition at 900 nm. The spectrum exhibits a strong and broad absorption band (240–400 nm) together with weak and narrow absorption lines at 396 and 440 nm. All these features correspond to Eu^{3+} absorption. The broad absorption band coincides with the well-known $S^{2-}\rightarrow Eu^{3+}$ CT absorption of Eu^{3+} in oxysulfides with an onset in the visible spectral region around 400 nm. The narrow absorption lines are assigned to 4f-4f transitions on Eu^{3+}: $^7F_{0,1}\rightarrow{}^5L_6$ (396 nm), $^7F_{0,1}\rightarrow{}^5D_2$ (440 nm). In addition, the characteristic Nd^{3+} excitation lines (including the lines around 600 nm) are present. As the excitation spectrum was monitored for Nd^{3+} emission and characteristic excitation bands/lines of Eu^{3+} were observed, it is evident that there is energy transfer between Eu^{3+} and Nd^{3+}. Also note that after co-doping with Eu^{3+}, the intensity of the 4f-4f excitation lines of Nd^{3+} (around 600 nm) is much lower than that of the Eu^{3+} CT band. This shows that successful sensitization of Nd^{3+} by Eu^{3+} was achieved.

To further investigate the Eu^{3+}-to-Nd^{3+} energy transfer efficiency, emission spectra were recorded under 340 nm excitation. As shown in Fig. 1**(d)**, several narrow emission lines can be observed between 500 and 700 nm, which are assigned to the Eu^{3+} $^5D_{0,1}\rightarrow{}^7F_{1\text{-}4}$ transitions, and lines between 800 and 1000 nm, which are assigned to Nd^{3+} $^4F_{5/2}\rightarrow{}^4I_{9/2}$ and $^4F_{3/2}\rightarrow{}^4I_{9/2}$ transitions. Furthermore, it can be observed that the dominant Eu^{3+} $^5D_0\rightarrow{}^7F_2$ emission is at 625 nm, consistent with Eu^{3+} in oxysulfides where this hypersensitive transition is typically observed around 625 nm [33,34].

The Eu^{3+} sensitizer concentration was varied to further optimize the sensitivity. The Fig. 1**(e)** shows the emission spectra of the Gd_2O_2S:yEu^{3+}, 0.008Nd^{3+} (y = 0.005, 0.008, 0.010, 0.015, 0.020). The emission intensity of Nd^{3+} at 823 nm and 900 nm increases gradually up to an Eu^{3+} concentration of 0.008 and decreases for higher Eu^{3+} concentrations. For higher Eu^{3+} doping concentration, the Nd^{3+} emission intensity gradually decreases again due to back transfer from Nd^{3+} to Eu^{3+} as the $^4F_{3/2}$-$^4I_{15/2}$ energy difference is almost resonant with the $^7F_0$-$^7F_6$ energy gap, causing a drop in Nd^{3+} $^4F_{3/2}$ emission intensity. Note that this Nd-Eu back transfer is not to the $^5D_0$ emitting level of Eu^{3+}. Co-doping with Eu^{3+} results in a higher emission intensity of Nd^{3+} while the emission spectra remained consistent compared with the single-doped sample (Fig. 1**(e)**). The optimum Eu^{3+}, Nd^{3+} co-doping concentration is 0.008Eu^{3+}, 0.008Nd^{3+} (Fig. 1**(f)**).

Additional evidence for the energy transfer between Eu^{3+} and Nd^{3+} is obtained from luminescence lifetime measurements.

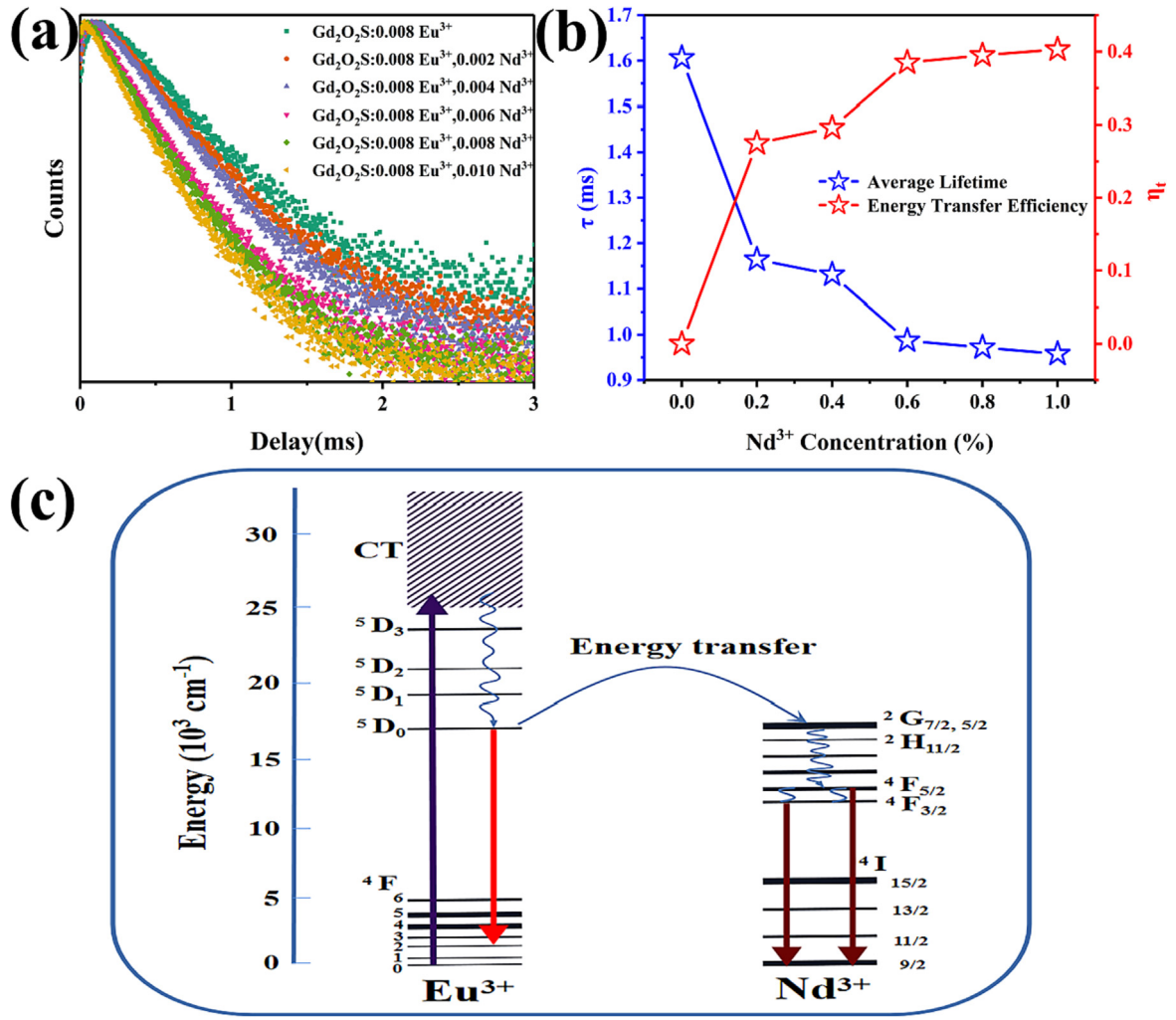

Fig. 2. (a) Luminescence decay curves of the Eu^{3+} emission for co-doped Gd_2O_2S:0.008Eu^{3+}, x Nd^{3+} ($0 \leq x \leq 0.01$) for λ_{ex} = 340 nm and λ_{em} = 625 nm at 300 K. (b) The average lifetime of Eu^{3+} and energy transfer efficiency between Eu^{3+} and Nd^{3+} with changing Nd^{3+} concentration. (c) The sensitization mechanism and temperature sensing of Gd_2O_2S:0.008Eu^{3+}, 0.008Nd^{3+} using Eu^{3+} charge transfer absorption (purple arrow) followed by relaxation to the ^5D_J states of Eu^{3+} and partial energy transfer to Nd^{3+}. Emission from the thermally coupled $^4F_{3/2}$ and $^4F_{5/2}$ levels (dark red arrows) of Nd^{3+} are used for Boltzmann thermometry in the lower temperature window (300–500 K) while the intensity ratio of the total Nd^{3+} (dark red arrows) to Eu^{3+} emission (red arrows) is used for accurate temperature sensing in the higher temperature window (500–650 K). (For interpretation of the references to colour in this figure legend, the reader is referred to the web version of this article.)

Fig. 2**(a)** depicts decay curves of Eu^{3+} emission at concentrations of Nd^{3+} varying from 0 to 0.01. The Eu^{3+} emission decay time becomes shorter with increasing of Nd^{3+} concentration. The emission decay curves are non-exponential as the local coordination with Nd^{3+} acceptors will vary. The average lifetimes τ were determined using [35]:

$$\tau = \frac{\int_{\infty}^{0} \boldsymbol{I_D(t)tdt}}{\int_{\infty}^{0} \boldsymbol{I_D(t)dt}} \quad (1)$$

where I_D (t) is the donor (Eu^{3+}) emission intensity at a time t. The average lifetime of Eu^{3+} emission for the co-doped samples decreases from 1.61 to 0.96 ms upon increasing the Nd^{3+} doping concentration to 1%. From these decay times, the energy transfer efficiency (η_t) can be calculated by the formula [36]:

$$\boldsymbol{\eta_t} = 1 - \frac{\tau}{\tau_0} \quad (2)$$

where τ_0 and τ refer to the lifetime of Eu^{3+} without and with co-doping of Nd^{3+} ions. The results show an increase of transfer efficiency up to ~ 40% for the highest Nd^{3+} concentration of 1% (Fig. 2**(b)**).

In summary, the luminescence mechanism of Gd_2O_2S co-doped with Eu^{3+} and Nd^{3+} is shown in Fig. 2**(c)** based on the above results. Red Eu^{3+} emission as well as NIR emission of Nd^{3+} are sensitized following strong CT absorption, relaxation to the $^5D_0$ level of Eu^{3+} and partial energy transfer from Eu^{3+} to Nd^{3+} when excited in the near UV. In the next section it will be demonstrated how the temperature dependence of this luminescence can be used for accurate temperature sensing over a wide temperature range.

Temperature-dependent luminescence. To investigate the temperature-dependent behavior of the $^4F_{3/2}$-$^4F_{5/2}$ luminescence of Nd^{3+}, emission spectra of Gd_2O_2S:0.008Nd^{3+} at elevated temperatures were monitored. Emission spectra were recorded at different temperatures between 298 and 623 K (Fig. 3**(a)** from red to yellow) with intervals of 25 K. As the temperature increases, the emission intensity of $^4F_{5/2}$-$^4I_{9/2}$ transition gradually increases, while that of the $^4F_{3/2}$-$^4I_{9/2}$ transition decreases (Fig. 3**(b)**). This behavior is well known and reflects the increase in thermal population of the $^4F_{5/2}$ level at elevated temperatures.

In Fig. 3**(c)** the natural logarithm of the $^4F_{5/2}$/$^4F_{3/2}$ LIR is plotted vs. the inverse temperature. For perfect Boltzmann equilibrium a straight line is expected. It is observed that in the low temperature

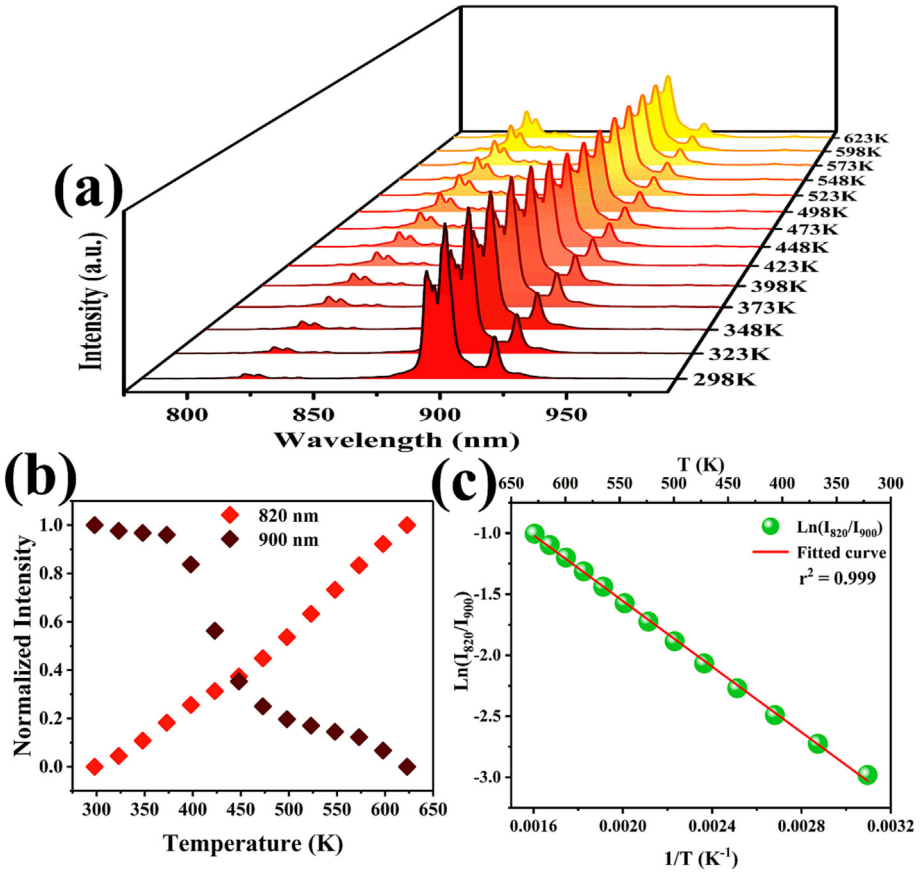

Fig. 3. (a) Temperature dependent emission spectra of Gd_2O_2S:0.008Nd^{3+} for 601 nm excitation. (b) Normalized integrated intensities of $^4F_{3/2}$-$^4I_{9/2}$ and $^4F_{5/2}$-$^4I_{9/2}$ emissions with temperature. (c) Ln (I_2/I_1) as function of 1/T – see also text.

range (below ~ 370 K) there is a small deviation indicating that Boltzmann equilibrium has not been established. Indeed, for Nd^{3+} with the large energy gap of about 1000 cm^{-1} between the $^4F_{3/2}$ and $^4F_{5/2}$ levels and the coupling by a magnetic dipole transition (instead of electric dipole) slows down thermal relaxation. It has been observed before for Nd^{3+} that thermal equilibration by phonon relaxation processes competes with depopulation through radiative decay and cross-relaxation of the $^4F_{3/2}$ and $^4F_{5/2}$ levels [25,37]. Depending on the host material and Nd^{3+} concentration, the onset of Boltzmann behavior (temperature at which equilibration rates start to outcompete population decay) can range from 300 to 450 K. The temperature-dependence of the LIR in the Boltzmann temperature regime was analyzed using Eq.(3) [38]:

$$\frac{I_2}{I_1} = Ce^{-\frac{\Delta E}{kT}} \quad (3)$$

Here I_i is the emission intensity from state i and C is a constant to correlate population and emission intensity ratios. The linear relation between Ln(I_2/I_1) and 1/T can be exploited as a calibration line for temperature sensing, as shown in Fig. 3**(c)**. Above 370 K Ln(I_2/I_1) shows a good linearity (r^2 = 0.999) with the inverse temperature, where I_2 is the integrated 790–850 nm emission intensity and I_1 is the integrated 860–940 nm emission intensity. The fitted equation obtained is Ln LIR = -1398/T + 1.24. From the fitting parameter for the slope (-1398) the $^4F_{3/2}$-$^4F_{5/2}$ energy gap is determined to be 972 cm^{-1}, in excellent agreement with the value determined from the excitation and emission spectra.

To extend the temperature range for thermal sensing, we explored temperature dependent energy transfer from Eu^{3+} to Nd^{3+} in addition to differences in thermal quenching behavior of the Nd^{3+} and Eu^{3+} emission and the temperature-dependent luminescence of Eu^{3+} and Nd^{3+} co-doped Gd_2O_2S was investigated. Fig. 4**(a)** shows the emission spectra of Gd_2O_2S:0.008Eu^{3+},0.008-Nd^{3+} at elevated temperatures (298–623 K, from red to yellow) under 340 nm excitation with temperature intervals of 25 K. After an initial slow decrease starting around 400 K, the emission intensity of Eu^{3+} $^5D_{0,1}$→$^7F_{1\text{-}4}$ transitions strongly drops above 450 K. This behavior can be explained by temperature dependence of the Eu^{3+} to Nd^{3+} energy transfer (becoming more efficient at higher temperatures) and thermal quenching of the Eu^{3+} emission above 450 K. Temperature quenching for Eu^{3+} [39,40] emission in oxysulfides has been extensively investigated in the past and shown to proceed via the low-lying CT state.

In addition to the Eu^{3+} emission, also Nd^{3+} emission is observed under CT excitation of Eu^{3+} as discussed in the previous section. As the temperature increases, the emission intensity of Nd^{3+} $^4F_{3/2}$-$^4I_{9/2}$ transition gradually decreases while that of the $^4F_{5/2}$-$^4I_{9/2}$ increases, similar to the observations in the singly Nd-doped material. The LIR again reflects the change in thermal population of the two levels. The integrated Nd^{3+} emission intensity ($^4F_{3/2}$+$^4F_{5/2}$) decreases when the thermal quenching of the Eu^{3+} sets in above 450 K. The Nd^{3+} emission is fed by energy transfer from Eu^{3+}. At room temperature radiative decay from the $^5D_0$ level of Eu^{3+} competes with energy transfer to Nd^{3+}, resulting in the energy transfer efficiencies around 40% reported above for 0.8% Nd^{3+} co-doping. When thermal quenching of the Eu^{3+} emission starts, energy transfer has to compete with radiative + non-radiative decay leading to an overall lower transfer efficiencies. As a result, the Nd^{3+} emission intensity decreases, albeit not as rapidly as the Eu^{3+} emission intensity.

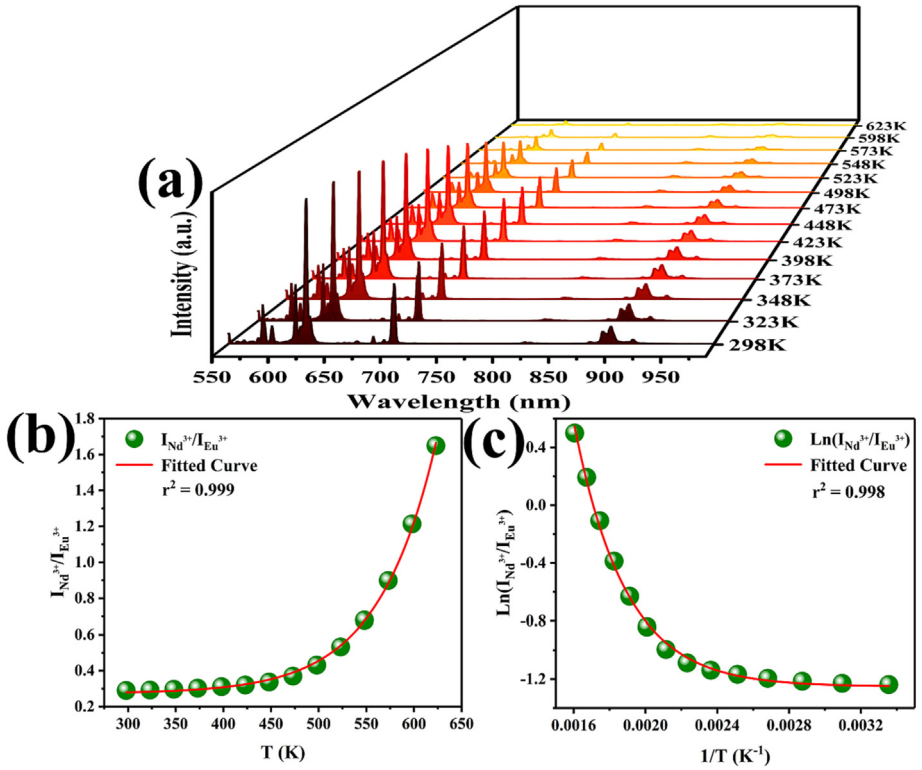

Fig. 4. (a) Temperature dependent emission spectra of Gd_2O_2S:0.008Eu^{3+}, 0.008Nd^{3+} for excitation at 340 nm. (b) Relationship between LIR (I^{3+}_{Nd}/I^{3+}_{Eu}) and T. (c) The relationship between Ln (I^{3+}_{Nd}/I^{3+}_{Eu}) and 1/T. Drawn lines are exponential fit curves of LIR vs. temperature and is not based on a physical model/description to explain the observed temperature dependence quantitatively.

The difference in thermal behavior of the Nd^{3+} and Eu^{3+} emission in the temperature regime above 450 K allows for temperature sensing based on the LIR of the Nd^{3+} to Eu^{3+} emission. The temperature dependence of this LIR is shown in Fig. 4**(b)**, where the (I^{3+}_{Nd}/I^{3+}_{Eu}) LIR is plotted versus temperature. Here I_{Nd3+} is the integrated intensity between 800 and 950 nm and I_{Eu3+} is the integrated intensity between 550 and 670 nm. Modelling the experimentally observed temperature dependence is complex. Several processes contribute, including temperature dependent energy transfer, thermal quenching of the Eu^{3+} emission and quenching of the Nd^{3+} emission by temperature dependent cross-relaxation. For proper modelling, also the (concentration dependent) variation in local distribution of Nd^{3+} ions around Eu^{3+} has to be taken into account and requires extensive additional studies. For the present study the experimentally observed (I^{3+}_{Nd}/I^{3+}_{Eu}) LIR vs. T was fitted to exponential function resulting in a good fit (r^2 = 0.999) in the tested temperature range (298 K – 623 K). The fitted equation obtained is LIR = 4.75*10^{-5}exp(T/60.58) + 0.27. Similarly, a plot of Ln(I_{Nd3+}/I_{Eu3+}) versus 1/T was obtained (Fig. 4**(c)**) and also here the fitted curve could be described by an exponential fit (r^2 = 0.998). The fitted equation obtained is Ln LIR = 490exp(-T/2.86*10^{-4}) – 1.25. These empirical fits can be used as calibration curves for temperature sensing. Note that, different from a single ion Boltzmann thermometer, the temperature dependence of the (I^{3+}_{Nd}/I^{3+}_{Eu}) LIR will strongly depend on the Eu^{3+} and Nd^{3+} concentrations (here 0.8% for both) and calibration curves are not generally valid but require specification of dopant concentrations. On the one hand this is a drawback, on the other hand doping concentrations can be varied to tune and optimize sensitivity in a specific temperature range similar to what has been realized in Tm^{3+}- and Ho^{3+}-based energy transfer thermometers [41,42].

Temperature sensing performance. To appreciate the performance of the novel dual functionality Gd_2O_2S: Eu^{3+}, Nd^{3+} thermometers the durability, accuracy, sensitivity and reproducibility are essential parameters to evaluate. To compare the performance of thermometers the relative sensitivity [43] is commonly used,

$$S_r = \frac{1}{LIR}\frac{dLIR}{dT} \quad (4)$$

S_r is used as a figure of merit to compare different temperature sensors, independent of the nature of the sensor and the measuring setup. As shown in Fig. 5**(a)**, the $^4F_{5/2}/^4F_{3/2}$ LIR relative sensitivity of Gd_2O_2S:0.008Nd^{3+} decreases with increasing temperature. This is typically observed for Boltzmann thermometers and limits the operational temperature range. The maximum relative sensitivity in the monitored temperature range is 1.5 %/K but S_r drops below 0.5%/K above 500 K. For the Gd_2O_2S:0.008Eu^{3+}, 0.008Nd^{3+} co-doped sample, the S_r for the (I^{3+}_{Nd}/I^{3+}_{Eu}) LIR increases with temperature, and sample reaches a maximum value of 1.4%/K at 623 K (Fig. 5**(b)**). Combining the $^4F_{5/2}/^4F_{3/2}$ LIR and (I^{3+}_{Nd}/I^{3+}_{Eu}) LIR allows for a high relative sensitivity (>0.6%/K) over the full 300 to 650 K temperature and strong absorption to realize a high brightness luminescence thermometer operating in a wide temperature range. Also, the absolute sensitivity (S_a) of Gd_2O_2S:0.008Nd^{3+} and Gd_2O_2S:0.008Eu^{3+}, 0.008Nd^{3+} as a function of temperature (see **Figure S5** and **Figure S6** for details) demonstrates the excellent sensitivity of the system, with a maximum absolute sensitivity of 2.3%/K (623 K). A comparison of the temperature sensing performance with singly Eu^{3+} or Nd^{3+} doped luminescent thermometers is given in **Table S2** showing the superior performance of the doubly doped material (see Supplementary Information for details). This makes our new dual functionality luminescence thermometer attractive for applications where an extended range of temperatures needs to be monitored with high accuracy [44–46].

Besides the relative sensitivity, the temperature uncertainty or temperature resolution and reproducibility of a temperature

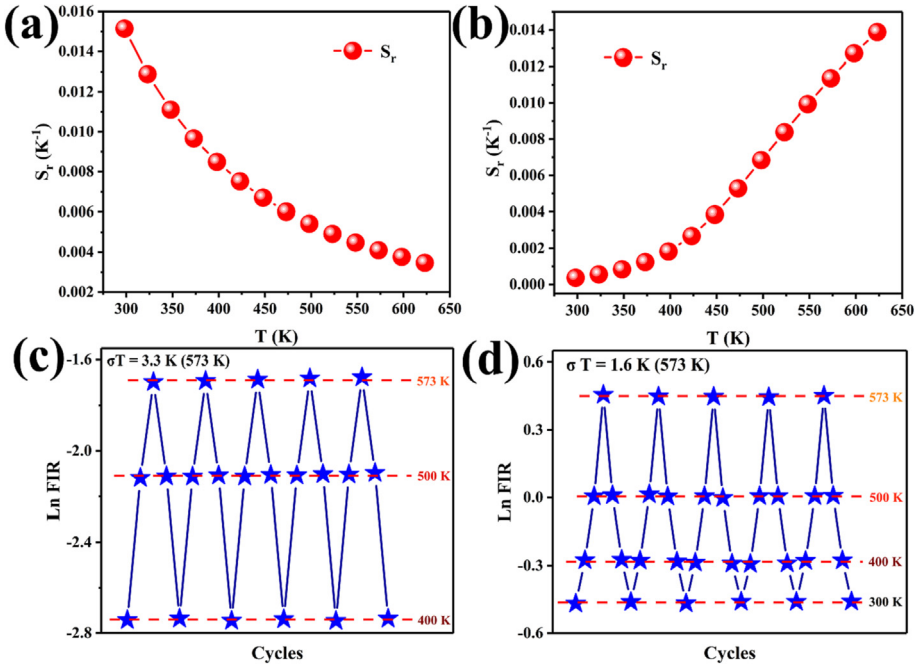

Fig. 5. (a) Relative sensitivities S_r as a function of temperature for temperature sensing based on the $^4F_{5/2}/^4F_{3/2}$ LIR in Gd_2O_2S:0.008Nd^{3+}. (b) Relative sensitivities as a function of temperature for temperature sensing based on the I^{3+}_{Nd}/I^{3+}_{Eu} LIR in Gd_2O_2S:0.008Eu^{3+},0.008Nd^{3+}. (c) Natural logarithm of the luminescence intensity ratio (Ln FIR) of $^4F_{5/2}/^4F_{3/2}$ for five consecutive heating and cooling cycles in Gd_2O_2S:0.008Nd^{3+}. (d) Natural logarithm of the luminescence intensity ratio (Ln FIR) of I^{3+}_{Nd}/I^{3+}_{Eu} for five consecutive heating and cooling cycles in Gd_2O_2S:0.008Eu^{3+},0.008Nd^{3+}.

sensor are essential parameters in order to fully characterize the thermometer. The actual temperature resolution and temperature uncertainty are also determined by the experimental conditions. In the case of low signals, poor signal-to-noise ratios can lead to large variations in the spectral readout and subsequently to a poor temperature resolution. The minimum temperature variation that can be measured under the real working conditions is given by [47,48],

$$\delta \mathbf{T} = \frac{\Delta \mathbf{FIR}}{\mathbf{FIR}} * \frac{1}{\boldsymbol{S_r}} \quad (5)$$

Here, the temperature uncertainty depends both on the relative uncertainty ΔFIR/FIR and on the relative sensitivity. While the theoretically optimum temperature accuracy can be calculated from S_r, it is also important to consider the brightness and the actual signal-to-noise obtained in the experiment. Low absorption strengths, reduced quantum yields, short acquisition times and poor light collection efficiencies are all experimental factors that will limit the actual temperature accuracy but are hard to predict as they depend on the specific temperature sensing application and experimental configuration.

For the Eu, Nd co-doped Gd_2O_2S the absorption strength (CT transition) and quantum yield are high and a good temperature accuracy can be expected. To investigate the temperature accuracy and reproducibility a series of thermal cycling experiments was performed. The results are shown in Fig. 5**(c)** and Fig. 5**(d)**. From the temperature variations the temperature uncertainty (δT, using equation (5) to calculate) of the Gd_2O_2S:0.008Nd^{3+} sample are calculated to be 1.0 K, 2.1 K and 3.3 K for 400 K, 500 K and 573 K in the 5 heating and cooling cycles, while the δT of Gd_2O_2S:0.008Eu^{3+}, 0.008Nd^{3+} are calculated to be 2.5 K, 2.2 K, 1.8 K and 1.6 K for 300 K, 400 K, 500 K and 573 K, respectively. This shows that the introduction of Eu^{3+} as a sensitizer into the gadolinium oxysulfide matrix extends the temperature range and reduces the temperature uncertainty. The excellent reproducibility observed in the various heating and cooling cycles for both Gd_2O_2S:0.008Nd^{3+} and Gd_2O_2S:0.008Eu^{3+}, 0.008Nd^{3+} samples also shows that these temperature probes have good durability and stability.

3. Multifunctional applications

Biological thermometry applications. The influence of temperature on the physiological processes of living cells is extremely significant [49]. In order to fully demonstrate the possibilities of the proposed materials for applications in the field of biosensing, cytotoxicity assays and cell imaging were carried out. For these experiments, Tongue squamous Cells (*T*-ca) were used. The results of the cell viability test indicated that after one day of treatment with Gd_2O_2S: Eu^{3+}, Nd^{3+} and Gd_2O_2S: Nd^{3+} (3.125–800 μg/mL), the cell viability is still over 92%, which is considered as almost non-toxic to living cells (Fig. 6**(a)**). Following that, after incubating for 6 h, 24 h, 48 h and 96 h with 200 μg/mL of Gd_2O_2S: Eu^{3+}, Nd^{3+}, bright fluorescence was visible in *T*-ca cells. The intracellular fluorescence intensity increased with increasing incubation time, being strongest at 24 h and then decreasing (Fig. 6**(b)**). This means that our materials can be successfully taken up by *T*-ca cells and fluorescence imaging can be obtained, implying great potential for use as a bio-probe for intracellular temperature detection.

In-situ temperature measurement in chemical reactors. The excellent performance of the Gd_2O_2S:Eu^{3+}, Nd^{3+} as a sensitive luminescence thermometer over a wide temperature range based on the results outlined makes our new dual functionality luminescence thermometer very promising candidates for applications where a wide temperature range needs to be monitored with high precision. In chemical reactors, monitoring the temperature distribution and even local temperature fluctuations is extremely important for optimising the reaction parameters. As shown in Fig. 7, we demonstrate the potential for luminescent temperature probe (*T*-probe) as an in-situ measurement technique in chemical

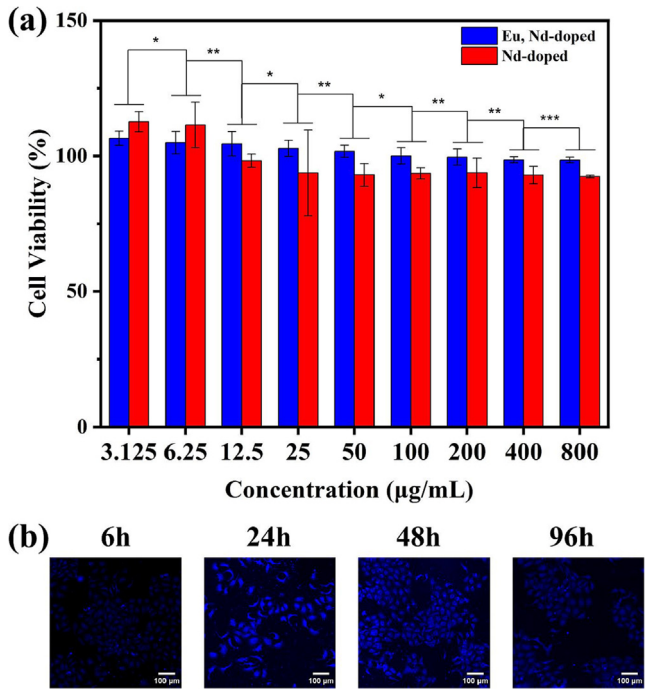

Fig. 6. (a) Cell viabilities of *T*-ca cells after culturing for 24 h with Gd_2O_2S: Eu^{3+}, Nd^{3+} and Gd_2O_2S: Nd^{3+} particles at indicated concentrations. (b) The fluorescence images of *T*-ca cells incubated with Gd_2O_2S: Eu^{3+}, Nd^{3+} for 6 h, 24 h, 48 h and 96 h.

reactors. Using inexpensive and powerful near-ultraviolet diodes and diode lasers as excitation sources, the luminescence spectra are output by a spectrometer that collects the optical signals and by means of known calibration curves the corresponding temperature changes or temperature distributions during the chemical reaction can be obtained.

4. Conclusion and outlook

The present results outline the excellent performance of Gd_2O_2S:0.008Eu^{3+},0.008Nd^{3+} as a sensitive luminescence thermometer over a wide temperature range (300–650 K) by utilizing the dual functionality of the LIR of thermally coupled $^4F_{5/2}/^4F_{3/2}$ levels of Nd^{3+} and the temperature dependence of the Nd^{3+} to Eu^{3+} emission intensity ratio. Furthermore, efficient sensitization is realized for near-UV excitation through strong broad band absorption in the Eu^{3+} charge transfer band, followed by partial energy transfer to Nd^{3+}. It is worth noting that it is not common for Eu^{3+} to be used as a sensitizer. These results make our new dual functionality luminescence thermometer attractive for multiple applications, where an extended range of temperatures needs to be monitored with high accuracy. In the low temperature region, the materials are non-toxic to cells and intracellularly imagerable, making them very promising candidates for biothermometry applications. In the higher or extended temperature region, our novel luminescence thermometer for in situ temperature measurement of chemical reaction processes also have great potential for application. Future research can aim to further explore the flexibility of this new thermometry system and tune and optimize the performance by varying the Eu^{3+} and Nd^{3+} concentrations and also by tuning the Eu^{3+} temperature quenching, for example by modifying the composition of the oxysulfide host to Y_2O_2S (higher T_Q for Eu^{3+}) or La_2O_2S (lower T_Q for Eu^{3+}). In addition, further research can be done into the mechanism behind the various temperature dependent processes contributing to model the experimentally observed changes in the (I^{3+}_{Nd}/I^{3+}_{Eu}) LIR. Finally, the concept presented here may initiate the design of other sensitized dual functionality luminescence thermometers to expand the capabilities of luminescence (nano) thermometry.

Associated Content

In the Supplementary Material Experimental Section, Structure and morphology including XRD patterns, refinement results of matrix, SEM, TEM and HRTEM images and EDX data, Detailed

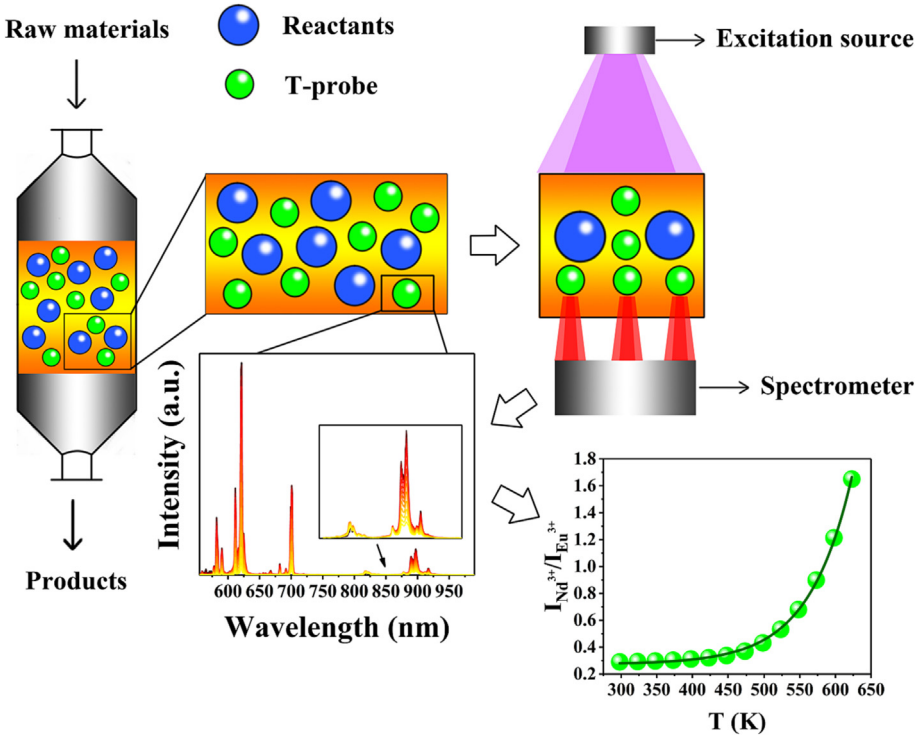

Fig. 7. Schematic overview of in-situ temperature measurement in a chemical reactor.

temperature-dependent emission spectra of Gd_2O_2S:0.008Eu^{3+}, 0.008Nd^{3+} excited at 340 nm are provided. In addition, figures for the temperature dependence of the absolute sensitivity are shown and a Table comparing the performance of singly Eu or Nd doped vs. doubly Eu, Nd doped thermometers is included.

CRediT authorship contribution statement

Yixuan Ma: Methodology, Software, Validation, Formal analysis, Investigation, Data curation, Writing – original draft. **Abida Aierken:** Investigation, Data curation. **Yuhua Wang:** Resources, Writing – review & editing, Supervision, Project administration, Funding acquisition. **Andries Meijerink:** Conceptualization, Formal analysis, Writing – original draft, Writing – review & editing, Supervision, Project administration, Funding acquisition.

Data availability

Data will be made available on request.

Declaration of Competing Interest

The authors declare that they have no known competing financial interests or personal relationships that could have appeared to influence the work reported in this paper.

Acknowledgements

This work was support from the National Natural Science Foundation of China (No. 52072163). We thank Prof. Qiyue Shao for his help with variable temperature spectroscopy and Prof. Jiahua Zhang for his help with temperature dependent spectroscopy.

Appendix A. Supplementary material

Supplementary data to this article can be found online at https://doi.org/10.1016/j.jcis.2023.02.022.

References

[1] S.W. Allison, G.T. Gillies, Remote thermometry with thermographic phosphors: Instrumentation and applications, Rev. Sci. Instrum. 68 (7) (1997) 2615–2650.
[2] P.R.N. Childs, J.R. Greenwood, C.A. Long, Review of temperature measurement, Rev. Sci. Instrum. 71 (8) (2000) 2959–2978.
[3] A.H. Khalid, K. Kontis, Thermographic phosphors for high temperature measurements: principles, current state of the art and recent applications, Sensors (Basel) 8 (9) (2008) 5673–5744.
[4] O.S. Wolfbeis, Sensor paints, Adv. Mater. 20 (19) (2008) 3759–3763.
[5] K.M. McCabe, M. Hernandez, Molecular thermometry, Pediatr Res 67 (5) (2010) 469–475.
[6] D. Jaque, L. Martinez Maestro, B. del Rosal, P. Haro-Gonzalez, A. Benayas, J.L. Plaza, E. Martin Rodriguez, J. Garcia Sole, Nanoparticles for photothermal therapies, Nanoscale 6 (16) (2014) 9494–9530.
[7] J.-C.-G. Bünzli, Lanthanide luminescence: from a mystery to rationalization, understanding, and applications, Including Actinides (2016) 141–176.
[8] S. Uchiyama, C. Gota, T. Tsuji, N. Inada, Intracellular temperature measurements with fluorescent polymeric thermometers, Chem Commun (Camb) 53 (80) (2017) 10976–10992.
[9] V.K. Rai, Temperature sensors and optical sensors, Appl. Phys. B 88 (2) (2007) 297–303.
[10] S. Uchiyama, A. Prasanna de Silva, K. Iwai, Luminescent molecular thermometers, J. Chem. Educ. 83 (5) (2006).
[11] C.D. Brites, P.P. Lima, N.J. Silva, A. Millan, V.S. Amaral, F. Palacio, L.D. Carlos, A luminescent molecular thermometer for long-term absolute temperature measurements at the nanoscale, Adv Mater 22 (40) (2010) 4499–4504.
[12] C.D. Brites, P.P. Lima, N.J. Silva, A. Millan, V.S. Amaral, F. Palacio, L.D. Carlos, Thermometry at the nanoscale, Nanoscale 4 (16) (2012) 4799–4829.
[13] D. Jaque, F. Vetrone, Luminescence nanothermometry, Nanoscale 4 (15) (2012) 4301–4326.
[14] X.D. Wang, O.S. Wolfbeis, R.J. Meier, Luminescent probes and sensors for temperature, Chem Soc Rev 42 (19) (2013) 7834–7869.
[15] M.D. Dramicanin, Sensing temperature via downshifting emissions of lanthanide-doped metal oxides and salts. A review, Methods Appl Fluoresc 4 (4) (2016) 042001.
[16] S.S. Laha, A.R. Naik, E.R. Kuhn, M. Alvarez, A. Sujkowski, R.J. Wessells, B.P. Jena, Nanothermometry measure of muscle efficiency, Nano Lett 17 (2) (2017) 1262–1268.
[17] M. Quintanilla, L.M. Liz-Marzán, Guiding rules for selecting a nanothermometer, Nano Today 19 (2018) 126–145.
[18] C.D.S. Brites, S. Balabhadra, L.D. Carlos, Lanthanide-based thermometers: at the cutting-edge of luminescence thermometry, Adv. Opt. Mater. 7 (5) (2018).
[19] L. Labrador-Paez, M. Pedroni, A. Speghini, J. Garcia-Sole, P. Haro-Gonzalez, D. Jaque, Reliability of rare-earth-doped infrared luminescent nanothermometers, Nanoscale 10 (47) (2018) 22319–22328.
[20] M. Runowski, S. Goderski, D. Przybylska, T. Grzyb, S. Lis, I.R. Martin, Sr_2LuF_7: Yb^{3+}–Ho^{3+}–Er^{3+} upconverting nanoparticles as luminescent thermometers in the first, second, and third biological windows, ACS Appl. Nano Mater. 3 (7) (2020) 6406–6415.
[21] H. Suo, C. Guo, Z. Yang, S. Zhou, C. Duan, M. Yin, Thermometric and optical heating bi-functional properties of upconversion phosphor $Ba_5Gd_8Zn_4O_{21}$: Yb^{3+}/Tm^{3+}, J. Mater. Chem. C 3 (28) (2015) 7379–7385.
[22] T. Li, C. Guo, H. Suo, P. Zhao, Dual-mode modulation of luminescence chromaticity in $AgLa(MoO_4)_2$: Yb^{3+}, Ho^{3+} up-conversion phosphors, J. Mater. Chem. C 4 (10) (2016) 1964–1971.
[23] E. Carrasco, B. Del Rosal, F. Sanz-Rodríguez, A.J. De La Fuente, P.H. Gonzalez, U. Rocha, K.U. Kumar, C. Jacinto, J.G. Solé, D. Jaque, Intratumoral thermal reading during photo-thermal therapy by multifunctional fluorescent nanoparticles, Adv. Funct. Mater. 25 (4) (2015) 615–626.
[24] M. Runowski, P. Woźny, S. Lis, V. Lavín, I.R. Martín, Optical vacuum sensor based on lanthanide upconversion—luminescence thermometry as a tool for ultralow pressure sensing, Adv. Mater. Technol. 5 (4) (2020) 1901091.
[25] M. Suta, Z. Antic, V. Ethordevic, S. Kuzman, M.D. Dramicanin, A. Meijerink, Making Nd^{3+} a sensitive luminescent thermometer for physiological temperatures-an account of pitfalls in Boltzmann thermometry, Nanomaterials (Basel) 10 (3) (2020).
[26] S. Anghel, S. Golbert, A. Meijerink, A.-V. Mudring, Divalent Europium doped CaF_2 and BaF_2 nanocrystals from ionic liquids, J. Lumin. 189 (2017) 2–8.
[27] B. Lei, Y. Liu, J. Zhang, J. Meng, S. Man, S. Tan, Persistent luminescence in rare earth ion-doped gadolinium oxysulfide phosphors, J. Alloy. Compd. 495 (1) (2010) 247–253.
[28] J.J. Dolo, O.M. Ntwaeaborwa, J.J. Terblans, E. Coetsee, B.F. Dejene, M.M. Biggs, H. C. Swart, The effect of oxygen pressure on the structure, morphology and photoluminescence intensity of pulsed laser deposited Gd_2O_2S:Tb^{3+} thin film phosphor, Appl. Phys. A 101 (4) (2010) 655–659.
[29] A.H. Khalid, K. Kontis, 2D surface thermal imaging using rise-time analysis from laser-induced luminescence phosphor thermometry, Meas. Sci. Technol. 20 (2) (2009).
[30] E.-J. Popovici, L. Muresan, A. Hristea-Simoc, E. Indrea, M. Vasilescu, M. Nazarov, D.Y. Jeon, Synthesis and characterisation of rare earth oxysulphide phosphors. I. Studies on the preparation of Gd_2O_2S: Tb phosphor by the flux method, Opt. Mater. 27 (3) (2004) 559–565.
[31] F. Wang, X. Chen, D. Liu, B. Yang, Y. Dai, Experimental and theoretical study of pure and doped crystals: Gd_2O_2S, Gd_2O_2S:Eu^{3+} and Gd_2O_2S:Tb^{3+}, J. Mol. Struct. 1020 (2012) 153–159.
[32] G. Li, Y. Wang, W. Zeng, W. Chen, S. Han, H. Guo, Y. Li, Photo-/cathodoluminescence and energy transfer properties of novel Ce^{3+} singly doped and Ce^{3+}/Tb^{3+} codoped $NaBaScSi_2O_7$ phosphors, J. Mater. Chem. C 4 (15) (2016) 3304–3312.
[33] S.A. Osseni, S. Lechevallier, M. Verelst, C. Dujardin, J. Dexpert-Ghys, D. Neumeyer, M. Leclercq, H. Baaziz, D. Cussac, V. Santran, R. Mauricot, New nanoplatform based on Gd_2O_2S:Eu^{3+} core: synthesis, characterization and use for in vitro bio-labelling, J. Mater. Chem. 21 (45) (2011).
[34] I.G.N. Silva, L.C.V. Rodrigues, E.R. Souza, J. Kai, M.C.F.C. Felinto, J. Hölsä, H.F. Brito, O.L. Malta, Low temperature synthesis and optical properties of the R_2O_3:Eu^{3+} nanophosphors (R^{3+}: Y, Gd and Lu) using TMA complexes as precursors, Opt. Mater. 40 (2015) 41–48.
[35] T. Zhou, L. Mei, Y. Zhang, L. Liao, H. Liu, Q. Guo, Color-tunable luminescence properties and energy transfer of Tb^{3+}/Sm^{3+} co-doped $Ca_9La(PO_4)_5(SiO_4)F_2$ phosphors, Opt. Laser Technol. 111 (2019) 191–195.
[36] F. Lahoz, I.R. Martin, J. Mendez-Ramos, P. Nunez, Dopant distribution in a Tm^{3+}-Yb^{3+} codoped silica based glass ceramic: an infrared-laser induced upconversion study, J Chem Phys 120 (13) (2004) 6180–6190.
[37] M. Suta, A. Meijerink, A theoretical framework for ratiometric single ion luminescent thermometers—thermodynamic and kinetic guidelines for optimized performance, Adv. Theory Simulat. 3 (12) (2020).
[38] G. Zhang, D. Wang, B. Lou, C.G. Ma, A. Meijerink, Y. Wang, Efficient broadband near-infrared emission from lead-free halide double perovskite single crystal, Angew Chem Int Ed Engl 61 (33) (2022) e202207454.
[39] C.W. Struck, W.H. Fonger, Quantum-mechanical treatment of Eu^{+3}4f→4fand 4f?charge-transfer-state transitions in Y_2O_2S and La_2O_2S, J. Chem. Phys. 64 (4) (1976) 1784–1790.
[40] L. van Pieterson, M. Heeroma, E. de Heer, A. Meijerink, Charge transfer luminescence of Yb^{3+}, J. Lumin. 91 (3–4) (2000) 177–193.
[41] E.C. Ximendes, A.F. Pereira, U. Rocha, W.F. Silva, D. Jaque, C. Jacinto, Thulium doped LaF_3 for nanothermometry operating over 1000 nm, Nanoscale 11 (18) (2019) 8864–8869.

[42] T.P. Swieten, D. Yu, T. Yu, S.J.W. Vonk, M. Suta, Q. Zhang, A. Meijerink, F.T. Rabouw, A Ho^{3+}-based luminescent thermometer for sensitive sensing over a wide temperature range, Adv. Opt. Mater. 9 (1) (2020).
[43] S.A. Wade, S.F. Collins, G.W. Baxter, Fluorescence intensity ratio technique for optical fiber point temperature sensing, J. Appl. Phys. 94 (8) (2003).
[44] M. Runowski, P. Woźny, N. Stopikowska, I.R. Martín, V. Lavín, S. Lis, Luminescent nanothermometer operating at very high temperature—sensing up to 1000 K with upconverting nanoparticles (Yb^{3+}/Tm^{3+}), ACS applied materials & interfaces 12(39) (2020) 43933-43941.
[45] T. Zheng, M. Sójka, M. Runowski, P. Woźny, S. Lis, E. Zych, Tm^{2+} activated SrB_4O_7 bifunctional sensor of temperature and pressure—highly sensitive, multi-parameter luminescence thermometry and manometry, Adv. Opt. Mater. 9 (22) (2021) 2101507.
[46] T. Zheng, M. Sójka, P. Woźny, I.R. Martín, V. Lavín, E. Zych, S. Lis, P. Du, L. Luo, M. Runowski, Supersensitive Ratiometric Thermometry and Manometry Based on Dual-Emitting Centers in Eu^{2+}/Sm^{2+}-Doped Strontium Tetraborate Phosphors, Advanced Optical Materials (2022) 2201055.
[47] S.N. Baker, T.M. McCleskey, G.A. Baker, An ionic liquid-based optical thermometer, ionic liquids IIIB: fundamentals, progress, Challenges, and Opportunities (2005) 171–181.
[48] C.D.S. Brites, A. Millán, L.D. Carlos, Lanthanides in luminescent thermometry, Including Actinides (2016) 339–427.
[49] A.M. Kaczmarek, M. Suta, H. Rijckaert, A. Abalymov, I. Van Driessche, A.G. Skirtach, A. Meijerink, P. Van Der Voort, Visible and NIR upconverting Er^{3+} – Yb^{3+} luminescent nanorattles and other hybrid PMO-inorganic structures for in vivo nanothermometry, Adv. Funct. Mater. 30 (32) (2020).